Handbook of Geospatial Approaches to Sustainable Cities

Edited by Qihao Weng in collaboration with Cheolhee Yoo

First published 2024

ISBN: 978-1-032-15481-7 (hbk)
ISBN: 978-1-032-15534-0 (pbk)
ISBN: 978-1-003-24456-1 (ebk)

6

Contrasting Pattern of Urban Expansion and Urban Land Use Intensification of Global Megacities using Nighttime Light Time Series Data

Qiming Zheng and Qihao Weng

DOI: 10.1201/9781003244561-8

The Open Access version of this chapter was funded by Qihao Weng.

CRC Press
Taylor & Francis Group
Boca Raton London New York

CRC Press is an imprint of the
Taylor & Francis Group, an **informa** business

6 Contrasting Pattern of Urban Expansion and Urban Land Use Intensification of Global Megacities using Nighttime Light Time Series Data

Qiming Zheng and Qihao Weng

INTRODUCTION

The world population, as reported by World Population Prospects 2019, is increasing towards 9.7 billion by 2050 (United Nations, 2019). The ongoing urbanization is projected to account for about 26% (2.5 billion) of the growth, whilst the urban dwellers will increase from 55% to 68% of the overall world's population by 2050 (Seto et al., 2017). This dramatic demographic transition, shifting population from rural to urban, is bringing a substantial, sophisticated and diverse changes to urban land cover and land use. These changes include: 1) urban growth, the conversion in the biophysical property of land cover, where natural landscapes, agricultural or forest lands are taken by built-up areas to fulfill the demand of urbanization (Gong et al., 2012); 2) urban land use intensification, also known as urban renewal, including cleaning out slums inside urban areas, and remodeling and/or reconstructing old infrastructures and buildings (e.g., brown-fields) into new uses (Stokes & Seto, 2019); 3) deurbanization, occurs whereby urban built-up areas are changed back to greens fields for conservation, recreation or other purposes (Satterthwaite et al., 2010); and (iv) urban land use degradation, highly developed urban areas being degraded into less developed areas, or even into vacant lands (Long & Wu, 2016).

The knowledge on the diversity of urban land changes is of high significance for understanding of urban environments and socio-economic changes. It has been well-documented that urban changes triggered a succession of repercussions on

DOI: 10.1201/9781003244561-8

local environment, human health and global climate change (Seto et al., 2012; Song et al.). Monitoring urban land changes in a spatially explicit and temporally intensive manner provides essential information for addressing these environmental issues (Batty, 2008; Weng, 2012). Understanding urban land changes is highly pertinent to the focus of Sustainable Development Goal 11, making cities and human settlement sustainable (Griggs et al., 2013; Guneralp et al., 2017), which requires information on urban land use and land cover, urban form and growth patterns, slums, buildings, transportation and infrastructure, green and public spaces, cultural and natural heritage sites.

The demands for more specific information on urban related uses pose new opportunities and challenges that require developing new geospatial methods to characterize different types of urban land changes. "Daytime" remote sensing (DRS) imagery, like Landsat or MODIS, can only present the biophysical attributes of earth's surface. Previous studies with DRS imagery have focused efforts on tracking a single type of urban land change, i.e., growth of urban extents (Song et al.; Zhu et al., 2019). Such unidimensional measurement largely ignores the other types of urban land changes, such as urban land use intensification and degradation, and deurbanization. Nighttime light (NTL) imagery provides a unique optical remote sensing data and is able to capture artificial light emitted at night with a global coverage (Román et al., 2018; Wang et al., 2021; Zheng et al., 2022).The detected NTL intensity is an integrated indication of both physical and socio-economic attributes of urban areas, so it may provide an alternative approach to disentangle and characterize different types of urban land changes (Stokes & Seto, 2019).

In this study, we disentangle urban land changes in 34 typical global megacities into the following types: urban growth (UG), deurbanization (DU), urban land use intensification (LUI), urban land use degradation (LUD) and no significant change (NC) by using the Visible Infrared Imaging Radiometer Suite (VIIRS) imagery of Suomi-NPP satellite.

STUDY AREA AND DATASETS

We have chosen 34 megacities as our study areas to represent a diverse range of factors, including urbanization status, urban size, climate, and landscape configuration (Figure 6.1). These megacities are typical representatives of current and

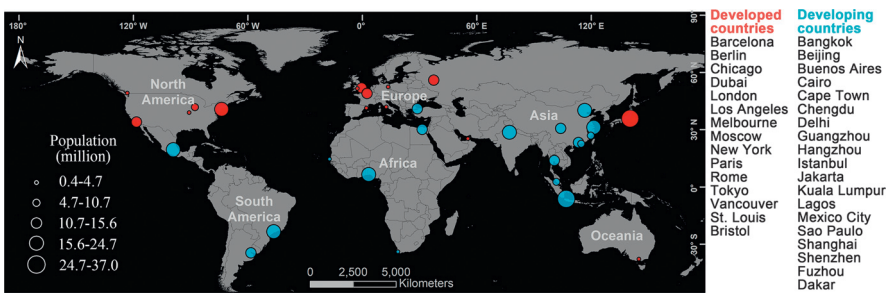

FIGURE 6.1 Study areas: 34 global megacities and the corresponding population.

projected urbanization hotspots, based on population data from 2016 and projections for 2030 (United Nations, 2016). Monitoring urban land changes in these megacities is crucial for understanding global urbanization trends and informing future development planning in less urbanized regions. We intentionally included megacities in tropical and sub-frigid areas, like Jakarta (6°N) and Moscow (55°N), to assess the robustness of our proposed method given different environmental conditions.

We utilized 84 monthly averaged VIIRS time series images, spanning from April 2012 to March 2019, to map urban changes. These images have a 15 arcsec spatial resolution and offer a high dynamic range (14 bit) and sensitive low light detection limit (2×10^{-11} W/cm2/sr) (Elvidge et al., 2017; Zhao et al., 2018). The VIIRS data consists of two datasets: average radiance (avg_rad) and the number of cloud-free observations (cf_cvg) used for calculating the avg_rad. Additionally, we obtained preprocessed data from the Google Earth Engine platform, including MODIS 16-Day NDVI (MOD13A1, 500 m), annual land cover maps (MCD12Q1, 500 m), and the Global Human Settlement Layer (GHSL), a 30-m resolution urban footprint map (Pesaresi et al., 2013).

METHODS

Figure 6.2 depicts the schematic flowchart of how we modeled and classified urban land change of the selected 34 megacities. We first used a Logistic-Harmonic model to fit monthly VIIRS NTL time series and then utilized the temporal features extracted from the fitted time series, together with a Random Forest classifier, to generate monthly urban built-up area maps. At last, we presented a post-classification scheme to categorize urban land change into five types: urban growth, deurbanization, urban land use intensification and degradation, and no change.

Time Series Modeling

We used a non-linear Logistic-Harmonic (LogH) model to fit the monthly VIIRS time series (Eq. 6.1 and Figure 6.3). The model captures the trend of NTL with a logistic term and models seasonality with two harmonic terms (Zheng et al., 2021).

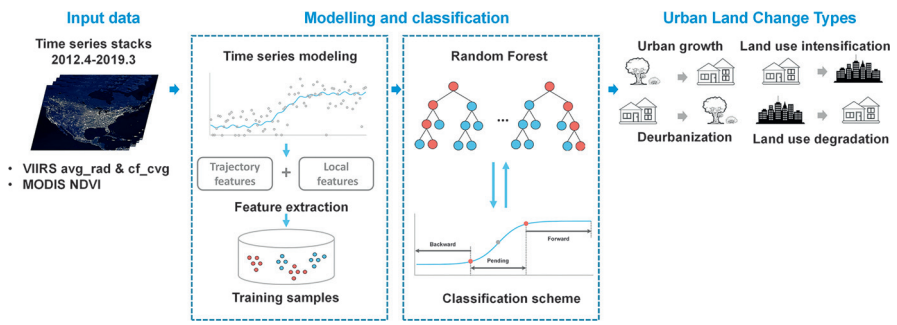

FIGURE 6.2 Methodological framework of this study.

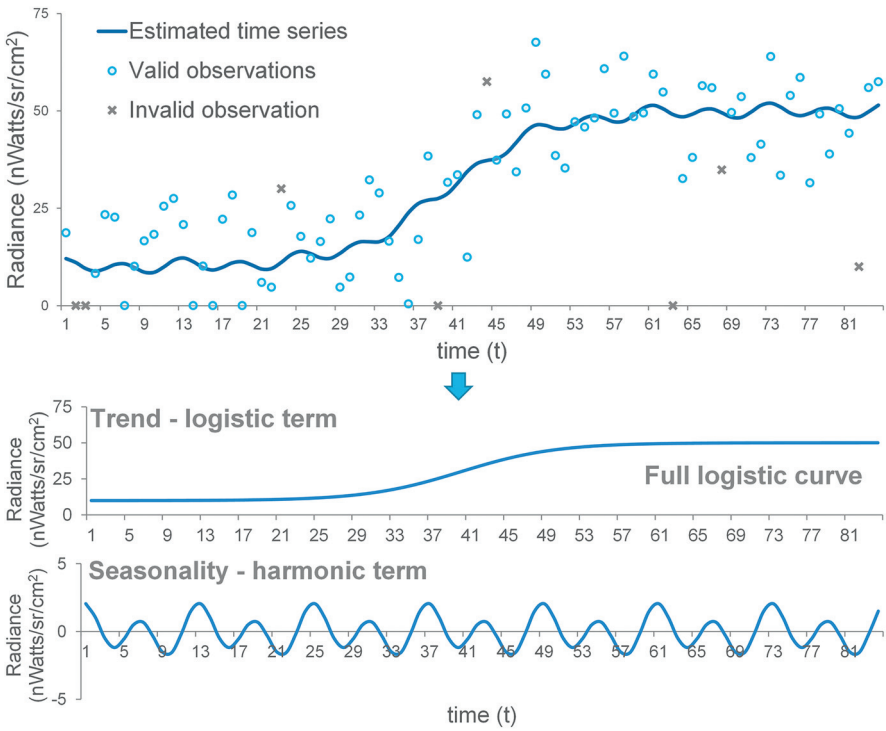

FIGURE 6.3 Illustrative figure of LogH model fitting.

The sigmoid function, known for its superiority in quantifying urban development stages and trajectory types, is suitable for NTL time series analysis and urban land change mapping (Song, 2016). The harmonic terms aim to offset the seasonality noises of NTL time series (Levin, 2017). The non-linear least square model with the Levenberg-Marquardt algorithm was used to estimate model parameters for each VIIRS pixel time series. We followed the approach proposed by Zheng et al. (2021) to screen out the impact from low-quality observations and estimate initial values for model parameters to ensure robust model performance.

$$Y_{log}(t) = \frac{a}{1 + \boldsymbol{e}^{bt+c}} + d + \sum_{k}^{2} \left[f_k \sin\left(\frac{2\pi kt}{12}\right) + g_k \cos\left(\frac{2\pi kt}{12}\right) \right] \tag{6.1}$$

where the estimated Y_{log} is a function of t (the t^{th} month of observation) with the following parameters: a (magnitude factor), b (change rate), c (timing of change), d (either pre-change or post-change radiance value), and f_k and g_k (amplitude factors of seasonality); $\boldsymbol{e}$ is the base of natural logarithm. The number of harmonic term k is set to 2 to account for the annual and semi-annual seasonal variation based on our previous study with the Lomb Scargle Periodogram test (Zheng et al., 2019). If a time series is not changed significantly or has a higher R^2 with a linear trend term, it will be fitted by a Linear-Harmonic model.

Urban Built-Up Area Mapping

We utilized the temporal information from the fitted trend of VIIRS NTL time series as input features, together with a Random Forest classifier, to create monthly urban built-up area maps. The trajectory shape of the trend term can vary significantly throughout the study period (t1 to t84), exhibiting a full logistic curve (Figure 6.4(a)), a partial curve covering a substantial portion (Figure 6.4(d)), or even a small portion (Figure 6.4(b)) of the full curve. However, using the estimated model parameters directly as input features would compromise classification accuracy (Gómez et al., 2016). To ensure robustness and stability, metrics and statistical features derived from time series trajectories were employed (Vogelmann et al., 2016). Our feature space consisted of trajectory features from the estimated trend term and local features from the target dates (Table 6.1). For VIIRS time, series data modeled by the Linear-Harmonic model or when tcp1, tcp2, or tcp3 fell outside the study period (t1 to t84), tcp1, tcp2, and tcp3 were set as t1, t42, and t84, respectively, to guarantee the quality and robustness of the extracted features.

Due to limited data availability, obtaining monthly stable training samples for global megacities with high-resolution data is not feasible. However, the MODIS MCD12Q1 land cover product provides a reliable 500 m built-up area map on a yearly basis since 2000 (Sulla-Menashe et al., 2019). To create stable training samples for each megacity, we randomly selected 500 built-up and 500 non-built-up pixels from the MCD12Q1 dataset. The sample selection followed specific criteria: 1) The selected pixel and its eight neighboring pixels belonged to the same land use/cover type throughout the study period. 2) To prevent spatial autocorrelation, no two samples were adjacent to each other. 3) For each megacity, 100 stable built-up and non-built-up samples were randomly chosen, and these samples were further

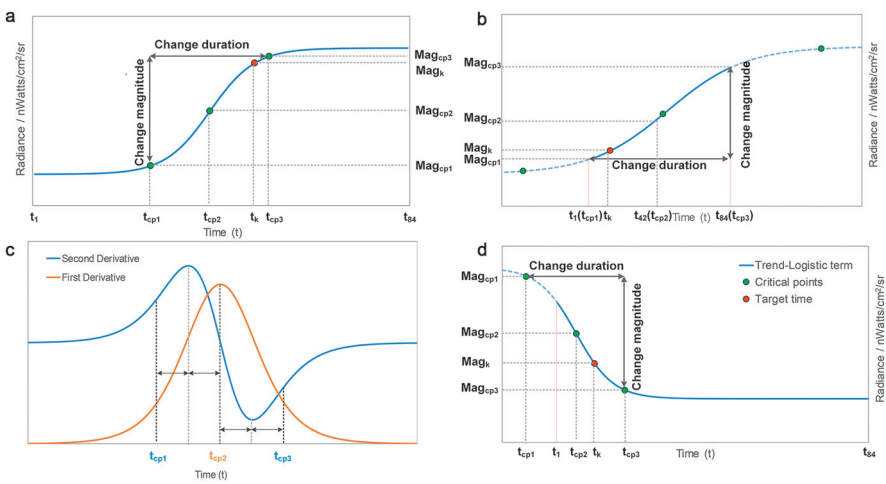

FIGURE 6.4 An illustrative diagram of NTL trajectory and local feature extraction. Full logistic term (a), and its first and second derivative (c); partial logistic curve (b) and (d).

TABLE 6.1
Explanation of Trajectory and Local Features

Trajectory Features	
Critical points 1 (CP1)	The start of change, $t_{CP1} = 2 \times t_{max}\text{-}t_{cp2}$
Critical points 2 (CP2)	The point with largest change rate, t_{cp2}
Critical points 3 (CP3)	The end of change, $t_{CP3} = 2 \times t_{min}\text{-}t_{cp2}$
NTL radiance of CPs	Mag_{cp1}, Mag_{cp2}, Mag_{cp3}
Change magnitude	$Change_{magnitude} = Mag_{cp3} - Mag_{cp1}$
Change duration	$Change_{duration} = \mid t_{cp3} - t_{cp1} \mid$
Change rate	$Change_{rate} = Change_{magnitude}/Change_{duration}$
Seasonality magnitude	$Seasonality_{magnitude} = \Sigma_k^2 \sqrt{f_k^2 + g_k^2}$
Local Features	
Time of target date	t_k
NTL radiance of target month	Mag_{tk}
Maximum NDVI (MOD13A1)	$NDVI_{max}$ is the maximum NDVI value within the 12 closest months of the target month (t_k)

validated using Google Earth images. If more than five inaccurate pixels were identified, all sample pixels were reselected.

At last, with the help of these stable training samples, we trained a Random Forest classifier each month and create monthly urban built-up areas maps. Classification accuracy was evaluated by calculating the out-of-bag accuracy score of the Random Forest (RF) algorithm and the overall accuracy. The reference data used for evaluation was obtained from the corresponding year's MCD12Q1 dataset. Additionally, a reference dataset was generated using GHSL, a medium spatial resolution built-up area map product, for a combined assessment. In this joint assessment, a VIIRS pixel of 500 m resolution was labeled as a built-up area if it contained more than 20% of the built-up area derived from GHSL.

Urban Land Change Classification and Analysis

We proposed a post-classification scheme to further categorize each pixel into five urban land change types: 1) urban land cover changes: urban growth (non-built-up area to built-up area) and deurbanization (built-up area to non-built-up area); 2) urban land use intensity changes: urban land use intensification (significant NTL intensity increase) and urban land use degradation (significant NTL intensity decrease); and 3) no statistically significant change (non-built-up to non-built-up or no significant NTL change) (Table 6.2).

At last, we analyzed the urban land change pattern of 34 selected megacities and compared the pattern across cities from developing countries and developed countries. We calculated the following metrics: 1) percentage of changed pixels

TABLE 6.2
Urban Land Change Types Identification

Pre-Change Stage	Post-Change Stage	Urban Land Change Types
Built-up	Built-up (NTL increasing)	Land use intensification
Non-built-up	Built-up	Urban growth (Land cover change)
Built-up	Non-built-up	Deurbanization (Land cover change)
	Built-up (NTL decreasing)	Land use degradation
Non-built-up	Non-built-up	No change
No significant change in NTL		No change

out of the total built-up area of each city; 2) percentage of each urban land change type of all changed pixels; and 3) average change magnitude of urban land use intensity, measured by changes in NTL radiance.

RESULTS

Time Series Modeling

Figure 6.5 summarizes the fitting performance for all pixels of 34 selected megacities. It presents: 1) the proportion of pixels fitted by the Linear-Harmonic model, the Logistic-Harmonic (LogH) model, and those that do not exhibit significant change (No change); 2) the mean R2 values; and 3) the mean normalized RMSE (nRMSE ∈ [0, 1]). Of the changed time series, approximately 90% were fitted by the LogH model, which demonstrated superior fitting performance (R2 = 0.51) compared to the Linear-Harmonic model (R2 = 0.30). The mean R2 of the LogH model ranged from 0.34 (Vancouver) to 0.66 (Delhi) across 34 megacities. The mean nRMSE for all cities ranged from 0 to 0.1. The LogH model exhibited a slightly higher mean nRMSE value (0.043) than the Linear-Harmonic model (0.027). This can be attributed to the LogH model capturing higher data variation in the fitted time series compared to the Linear-Harmonic model.

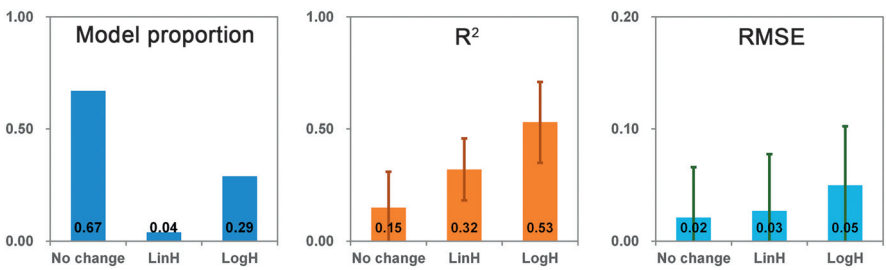

FIGURE 6.5 Results of time series modeling, including the proportion of model types, R2 and RMSE.

Urban Built-Up Area Mapping

Our method exhibited high consistency with MCD12Q1 and slightly lower agreement with GHSL. Discrepancies primarily occurred in scattered and low-density human settlements at urban outskirts and intercity highways. Table 6.3 compares the accuracy of our proposed method (Model 1) with other widely used nighttime light studies (Model 3–5). Temporal feature-based methods (Model 1&2) achieved higher overall accuracy, improving by up to 20%, compared to spectral-based methods (Model 3–5). By incorporating temporal features and NDVI, our proposed method (Model 1) achieved the highest accuracy of 97% (MCD12Q1 data) or 88% (GHSL data). Mapping accuracy varied at the city level, ranging from 93% (MCD12Q1) or 86% (GHSL) in Guangzhou, China, to 98% (MCD12Q1) or 92% (GHSL) in Sao Paolo, Brazil.

Figure 6.6 compares built-up areas identified by our method (Model 1), the NTL thresholding method (Model 4), and the spectral feature-based method (Model 5). Our temporal feature-based approach excels in handling heterogeneous landscapes. In cities dominated by built-up pixels like Shanghai (Figure 6.6(b)) and Melbourne (Figure 6.6(f)), Model 1 outperforms Model 4 by 6–12% (MCD12Q1) or Model 5 by 9–16% (GHSL) in accuracy (Table 6.3). This advantage is even more significant in cities with highly heterogeneous built-up/non-built-up landscapes such as Hangzhou (Figure 6.6(a)) and Bangkok (Figure 6.6(d)), where Model 1 surpasses Model 4 by 10–17% (MCD12Q1) or Model 5 by 11–23% (GHSL) in overall accuracy. This advantage applies to both urban outskirts and inner-city areas. For instance, in the Central Ridge Forest Reserve in downtown Delhi, India (Site 1 in Figure 6.6(b)), surrounded by commercial and public infrastructure, scenic spots, and a busy road, Model 4 and Model 5 fail to distinguish the forest reserve from the surrounding built-up

TABLE 6.3
Accuracy Assessment of Different Models

Methods		Features		References	
Models	**Type**	**Type**	**Feature Sets**	**MCD12Q1**	**GHSL**
1	Classification	Temporal	Temporal features; NDVI	96.9%	88.4%
2	Classification	Temporal	Temporal features	95.0%	87.3%
3	Thresholding	Spectral	VIIRS	72.1%	72.5%
4	Thresholding	Spectral	VANUI	84.6%	77.7%
5	Classification	Spectral	VIIRS; NDVI	85.7%	80.9%

Note: The accuracy yielded with MCD12Q1 indicates the average overall accuracy of all megacities for the 84 months; GHSL evaluates the accuracy of the built-up area map in December 2014 only. **Model 1** is the proposed method. **Model 3–5** are three widely-adopted methods, including thresholding method using raw VIIRS data (Model 3) (Liu et al., 2012) or a NTL index—VANUI* (Model 4) (Zhang et al., 2013), and classification-based method (Model 5) (Dou et al., 2017).

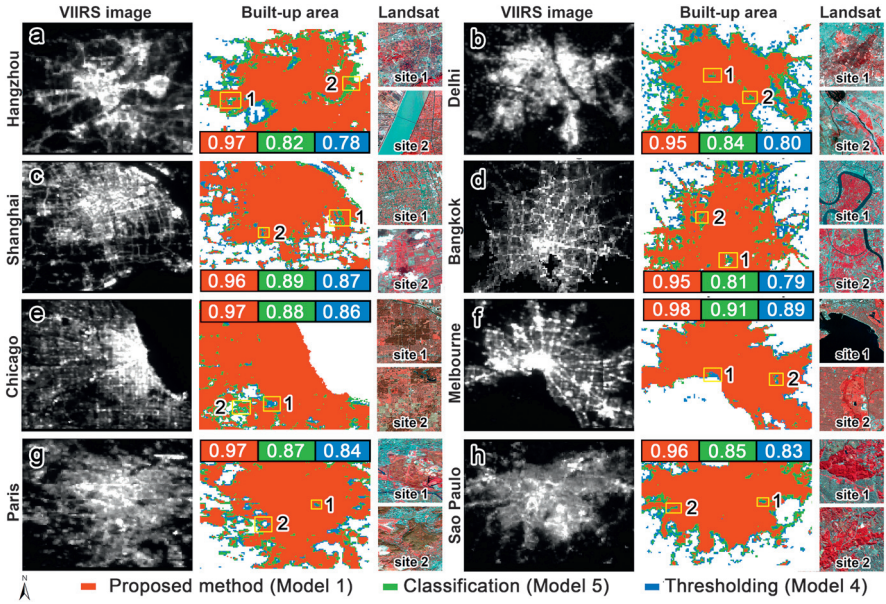

FIGURE 6.6 The left panel is VIIRS image; the middle panel is built-up areas derived by three different types of methods and the corresponding accuracy; the right panel is the zoomed-in Landsat images. (a-h) See text for details.

areas despite a moderate NTL intensity (18 nW/cm2/sr). In contrast, by using temporal features alone (Model 2) or in combination with NDVI (Model 1), a substantial portion of the forest reserve can be successfully identified as non-built-up areas. Another example is the outskirts of Chicago, USA (Site 2 in Figure 6.6(e)), where residential houses coexist with cropland and bare land. Model 1 demonstrates significantly higher accuracy in mapping built-up areas compared to other models.

Urban Land Change Pattern

Using accurate monthly built-up area maps, we categorized urban land change into five types: no change (NC), urban growth (UG), urban land use intensification (LUI), urban land use degradation (LUD), and deurbanization (DU). We analyzed urban land change patterns across 34 megacities (Figure 6.7) and found significant changes in over 53% of urban built-up pixels, varying across cities (11% in Berlin to 59% in Buenos Aires and 89% in Jakarta). Urban land use intensification (84%) and degradation (3%) accounted for the majority of changes, while urban growth represented only 4%. By distinguishing urban core and outskirts, we observed that urban growth, deurbanization, and land use degradation occurred primarily in the outskirts, while land use intensification and no change were evenly distributed.

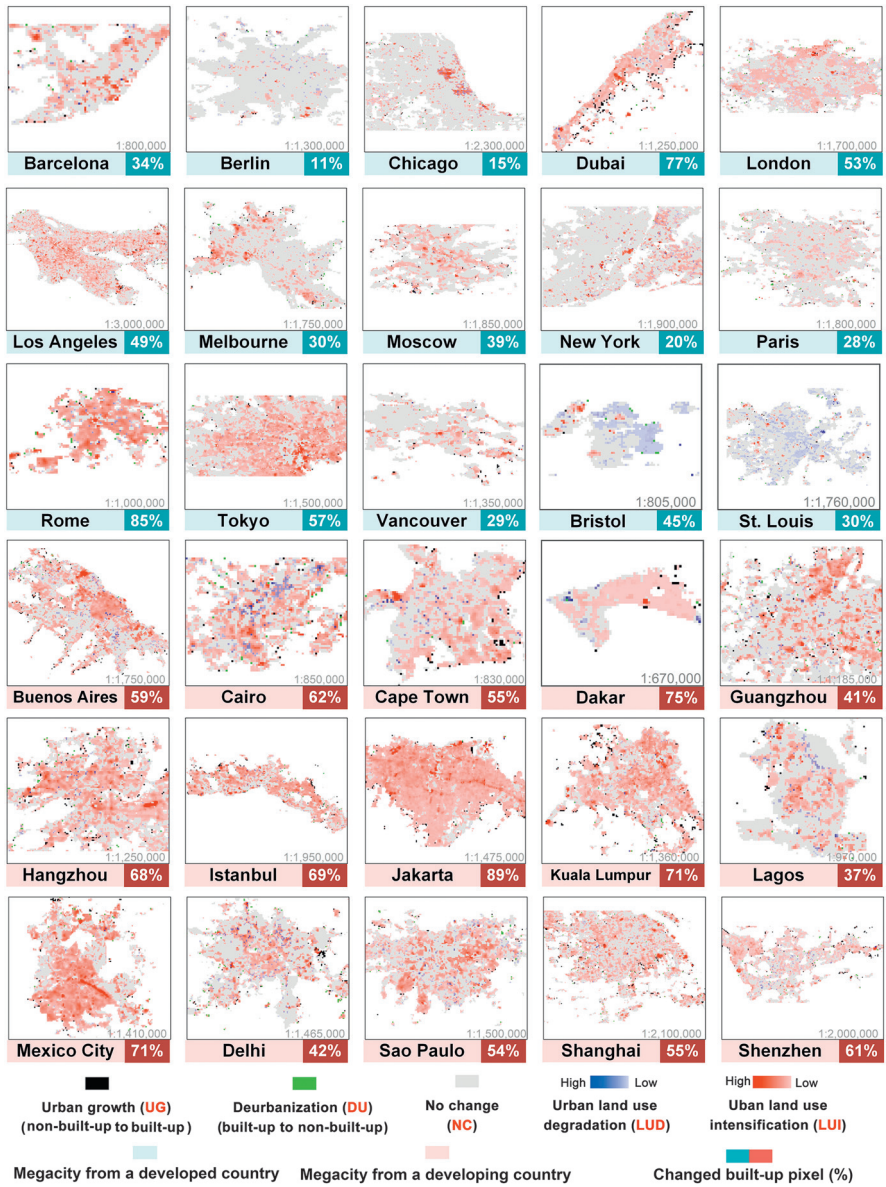

FIGURE 6.7 Urban land change types of 30 megacities. The percentage indicates the proportion of changed pixels in urban built-up areas. For better illustration, we only present the results of 30 out of 34 studied megacities.

Distinct urban change patterns emerged between developed and developing country megacities (Figure 6.8). Developing country megacities were more likely to follow a logistic urban development trajectory (50% compared to 30% in developed countries) and experienced a higher extent of urban land change (60% of pixels

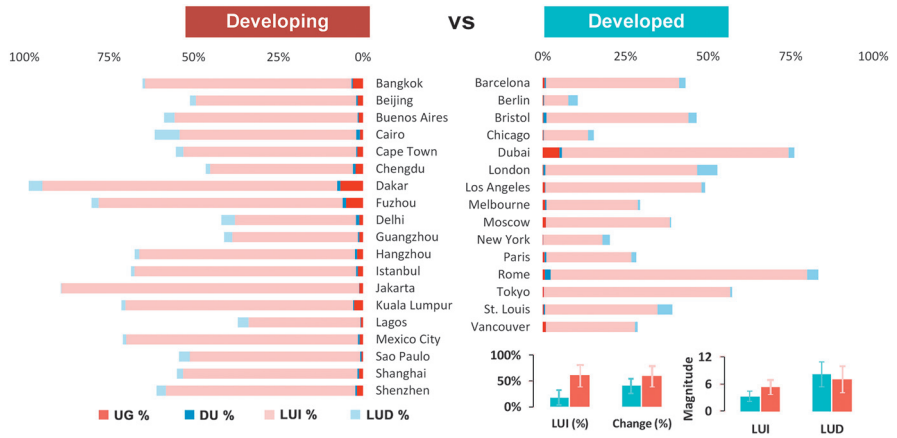

FIGURE 6.8 Urban land change types (%) of 34 megacities and comparison between megacities from developed and developing countries in terms of LUI (%), changed built-up pixels (%) and change magnitude of LUI and LUD.

compared to 39% in developed countries). Coastal megacities in Southeast Asia and Africa, such as Jakarta, Nairobi, and Kuala Lumpur, exhibited notable urban change. Developing country megacities underwent a higher proportion (63%) of urban land use change, including intensification and degradation, compared to developed country megacities (18%). In terms of magnitude, developing country megacities displayed higher land use intensification (5.8 nW/cm^2/sr) and lower land use degradation (−8.2 nW/cm^2/sr) than developed country megacities (3.0 nW/cm^2/sr and −6.5 nW/cm^2/sr, respectively).

DISCUSSIONS

In this study, temporal features derived from monthly VIIRS time series were used for urban built-up area mapping. Compared with traditional spectral-based methods, the advantages of the proposed method lied in the following aspects. First, spectral-based thresholding and classification methods depend only on the spectral value of a pixel, so they cannot effectively distinguish non-built-up areas with moderate or high NTL values from built-up areas, such as Site 1 in Figure 6.6(b). On the contrary, the NTL trajectories of built-up and non-built-up areas could vary significantly and thus are beneficial to differentiate them (Gómez et al., 2016; Zhu, 2017). This explains the high mapping accuracy of our method in non-built-up areas around urban outskirts and inside urban areas, where accommodate substantial moderate and extremely high NTL value pixels (Figure 6.6). Second, fitting time series model allows to isolate "noises" in VIIRS time series, e.g., the seasonal effect and ephemeral signals, so that the temporal pattern can be better modeled. Third, the use of dense monthly VIIRS time series can track gradual changes as well as subtle and abrupt changes. These changes would be buried in annual NTL time series or land cover map products that are released at an annual or 5–10 year interval and with a

lag of 1 to 2 years, such as GlobeLand30, GHSL and Global Urban Footprint (Esch et al., 2017; Pesaresi et al., 2013).

This study provides valuable insights into the temporal dynamics of urban land change, including types, spatial extent, intensity, and trend trajectories. These findings are crucial for advancing sustainable urban development goals. Two key implications emerge from our results. Firstly, while previous remote sensing studies have predominantly focused on urban growth, our analysis highlights the significance of land use intensification (84%) in shaping urban landscapes. This suggests a potential shift towards intensified land use in global megacities, necessitating further investigation into its environmental implications, such as impacts on urban ecosystems, local climate, energy consumption, and population distribution. Secondly, a notable distinction in urban land change patterns emerges between megacities in developing and developed countries. This disparity offers valuable insights for urban spatial planning, particularly in developing countries undergoing rapid urbanization, as they can draw lessons from the experiences of developed countries and their urban land trajectories.

Our proposed method has several limitations that should be acknowledged. Firstly, the presence of mixed pixels within the VIIRS imagery poses a challenge in accurately identifying land cover and land use changes within a single pixel. Due to the coarse resolution of VIIRS images, it is difficult to address this issue effectively. Additionally, the relationship between NTL intensity and specific urban land use types varies greatly across different regions, making it challenging to account for this variability. Secondly, our method assumes that there is only one dominant urban change type occurring during the study period within each pixel. However, in rare cases, consecutive urban land changes may occur, such as urban growth followed by urban land use intensification. This violates the premise of our approach and can result in difficulties in time series fitting and subsequent urban change mapping. Nevertheless, such cases were extremely rare in the selected megacities (<0.01%). Thirdly, the spectral range of VIIRS is limited to 500 nm to 900 nm, which means that certain types of light, such as that emitted by LEDs, cannot be detected. The exact contribution and how to compensate for this missing portion of light require further investigation. Lastly, although there are two coarse resolution NTL datasets available, DMSP-OLS and VIIRS, our study exclusively utilized VIIRS time series. This choice is due to the absence of an onboard calibration system in DMSP-OLS and its incompatibility with VIIRS. Despite recent efforts to harmonize DMSP-OLS and VIIRS, consistent time series in radiance values have not yet been achieved. These limitations should be considered in the interpretation and application of our method to ensure the accuracy and reliability of the results. Future research can focus on addressing these challenges to further improve urban land change mapping.

CONCLUSIONS

The study developed an effective method to analyze urban land changes in 30 global megacities. The proposed Logistic-Harmonic model demonstrated robust

performance in fitting monthly VIIRS time series, enabling the creation of accurate monthly built-up area maps and classification of urban land change types. The method achieved high overall accuracy when compared to MCD12Q1 (97%) or GHSL (88%), highlighting the superiority of temporal features over spectral features, particularly in heterogeneous regions. Additionally, the method improved temporal consistency and classification efficiency. Urban land changes were observed in 53% of built-up pixels, with urban land use intensification dominating (84%) the total urban changes over other urban land type, such as urban growth (4%). Megacities in developing countries exhibited wider extent and higher magnitude of urban land change, as well as a larger proportion of land use intensification compared to developed countries.

Further investigation is warranted in several areas. Firstly, exploring the potential of extending the Logistic-Harmonic model and temporal feature-based classification method to the upcoming Black Marble Product Suite, a high-quality daily VIIRS dataset with advanced correction processes, could provide valuable insights into urban land changes over time. Secondly, while our method demonstrated robustness against noise and low-quality observations, its applicability to different cities worldwide, and the potential for modeling other types of remote sensing time series data (e.g., reflectance or spectral indices) should be investigated. Additionally, calibrating DMSP-OLS and VIIRS would enable the examination of urban land cover and land use changes over longer time periods, offering further insights into urban dynamics.

REFERENCES

Batty, M. (2008). The size, scale, and shape of cities. *Science*, 319(5864), 769–771. 10.1126/science.1151419

Dou, Y., Liu, Z., He, C., & Yue, H. (2017). Urban Land Extraction Using VIIRS Nighttime Light Data: An Evaluation of Three Popular Methods. *Remote Sensing*, 9(2), 175. https://doi.org/10.3390/rs9020175

Elvidge, C., Baugh, K., Zhizhin, M., Hsu, F. C., & Ghosh, T. (2017). VIIRS night-time lights [1]. *International Journal of Remote Sensing*, 38(21), 5860–5879. 10.1080/01431161.2017.1342050

Esch, T., Heldens, W., Hirner, A., Keil, M., Marconcini, M., Roth, A., … Strano, E. (2017). Breaking new ground in mapping human settlements from space – The Global Urban Footprint. *ISPRS Journal of Photogrammetry and Remote Sensing*, 134, 30–42. 10.1016/j.isprsjprs.2017.10.012

Gómez, C., White, J. C., & Wulder, M. A. (2016). Optical remotely sensed time series data for land cover classification: A review. *ISPRS Journal of Photogrammetry and Remote Sensing*, 116, 55–72. 10.1016/j.isprsjprs.2016.03.008

Gong, P., Liang, S., Carlton, E. J., Jiang, Q., Wu, J., Wang, L., & Remais, J. V. (2012). Urbanisation and health in China. *The Lancet*, 379(9818), 843–852.

Griggs, D., Stafford-Smith, M., Gaffney, O., Rockström, J., Öhman, M. C., Shyamsundar, P., … Noble, I. (2013). Policy: Sustainable development goals for people and planet. *Nature*, 495(7441), 305.

Guneralp, B., Zhou, Y., Urge-Vorsatz, D., Gupta, M., Yu, S., Patel, P. L., … Seto, K. C. (2017). Global scenarios of urban density and its impacts on building energy use through 2050. *Proc Natl Acad Sci U S A*, 114(34), 8945–8950. 10.1073/pnas.1606035114

Levin, N. (2017). The impact of seasonal changes on observed nighttime brightness from 2014 to 2015 monthly VIIRS DNB composites [1]. *Remote Sensing of Environment*, 193, 150–164. 10.1016/j.rse.2017.03.003

Liu, Z., He, C., Zhang, Q., Huang, Q., & Yang, Y. (2012). Extracting the dynamics of urban expansion in China using DMSP-OLS nighttime light data from 1992 to 2008. *Landscape and Urban Planning*, 106(1), 62–72. https://doi.org/10.1016/j.landurbplan.2012.02.013

Long, Y., & Wu, K. (2016). Shrinking cities in a rapidly urbanizing China. *Environment and Planning A*, 48(2), 220–222.

Pesaresi, M., Huadong, G., Blaes, X., Ehrlich, D., Ferri, S., Gueguen, L., … Lu, L. (2013). A global human settlement layer from optical HR/VHR RS data: concept and first results. *IEEE Journal of Selected Topics in Applied Earth Observations and Remote Sensing*, 6(5), 2102–2131.

Román, M. O., Wang, Z., Sun, Q., Kalb, V., Miller, S. D., Molthan, A., … Masuoka, E. J. (2018). NASA's Black Marble nighttime lights product suite. *Remote Sensing Of Environment*, 210, 113–143. 10.1016/j.rse.2018.03.017

Satterthwaite, D., McGranahan, G., & Tacoli, C. (2010). Urbanization and its implications for food and farming. *Philosophical Transactions of the Royal Society B: Biological Sciences*, 365(1554), 2809–2820.

Seto, K. C., Golden, J. S., Alberti, M., & Turner, B. L., 2nd. (2017). Sustainability in an urbanizing planet. *Proceedings of the National Academy of Sciences U S A*, 114(34), 8935–8938. 10.1073/pnas.1606037114

Seto, K. C., Guneralp, B., & Hutyra, L. R. (2012). Global forecasts of urban expansion to 2030 and direct impacts on biodiversity and carbon pools. *Proceedings of the National Academy of Sciences U S A*, 109(40), 16083–16088. 10.1073/pnas.1211658109

Song, X. (2016). Characterizing themagnitude, timing and duration of urban growth from time series of Landsat-based estimates of impervious cover. *Remote Sensing of Environment*, 175, 1–13. 10.1016/j.rse.2015.12.027

Song, X. P., Hansen, M. C., Stehman, S. V., Potapov, P. V., Tyukavina, A., Vermote, E. F., & Townshend, J. R. (2018). Global land change from 1982 to 2016. *Nature*, 560(7720), 639–643.

Stokes, E. C., & Seto, K. C. (2019). Characterizing urban infrastructural transitions for the Sustainable Development Goals using multi-temporal land, population, and nighttime light data. *Remote Sensing Of Environment*, 234. 10.1016/j.rse.2019.111430

Sulla-Menashe, D., Gray, J. M., Abercrombie, S. P., & Friedl, M. A. (2019). Hierarchical mapping of annual global land cover 2001 to present: The MODIS Collection 6 Land Cover product. *Remote Sensing of Environment*, 222, 183–194. 10.1016/j.rse.2018.12.013

United Nations. (2016). The world's cities in 2016, data booklet. In: United Nations.

United Nations. (2019). World Population Prospects 2019, Online Edition. Retrieved from https://population.un.org/wpp/

Vogelmann, J. E., Gallant, A. L., Shi, H., & Zhu, Z. (2016). Perspectives on monitoring gradual change across the continuity of Landsat sensors using time-series data. *Remote Sensing of Environment*, 185, 258–270. 10.1016/j.rse.2016.02.060

Wang, Z., Román, M. O., Kalb, V. L., Miller, S. D., Zhang, J., & Shrestha, R. M. (2021). Quantifying uncertainties in nighttime light retrievals from Suomi-NPP and NOAA-20 VIIRS Day/Night Band data [1]. *Remote Sensing of Environment*, 263, 112557. 10.1016/j.rse.2021.112557

Weng, Q. (2012). Remote sensing of impervious surfaces in the urban areas: Requirements, methods, and trends. *Remote Sensing of Environment*, 117, 34–49. 10.1016/j.rse.2011.02.030

Zhang, Q., Schaaf, C., & Seto, K. C. (2013). The Vegetation Adjusted NTL Urban Index: A new approach to reduce saturation and increase variation in nighttime luminosity. *Remote Sensing of Environment*, 129, 32–41. https://doi.org/10.1016/j.rse.2012.10.022

Zhao, N., Zhang, W., Liu, Y., Samson, E. L., Chen, Y., & Cao, G. (2018). Improving Nighttime Light Imagery With Location-Based Social Media Data [1]. *IEEE Transactions on Geoscience and Remote Sensing*, 1–12. 10.1109/tgrs.2018.2871788

Zheng, Q., Weng, Q., & Wang, K. (2019). Developing a new cross-sensor calibration model for DMSP-OLS and Suomi-NPP VIIRS night-light imageries [1]. *ISPRS Journal of Photogrammetry and Remote Sensing*, 153, 36–47. 10.1016/j.isprsjprs.2019.04.019

Zheng, Q., Weng, Q., & Wang, K. (2021). Characterizing urban land changes of 30 global megacities using nighttime light time series stacks [1]. *ISPRS Journal of Photogrammetry and Remote Sensing*, 173, 10–23. 10.1016/j.isprsjprs.2021.01.002

Zheng, Q., Weng, Q., Zhou, Y., & Dong, B. (2022). Impact of temporal compositing on nighttime light data and its applications [1]. *Remote Sensing of Environment*, 274, 113016. 10.1016/j.rse.2022.113016

Zhu, Z. (2017). Change detection using landsat time series: A review of frequencies, preprocessing, algorithms, and applications. *ISPRS Journal of Photogrammetry and Remote Sensing*, 130, 370–384. 10.1016/j.isprsjprs.2017.06.013

Zhu, Z., Zhou, Y., Seto, K. C., Stokes, E. C., Deng, C., Pickett, S. T. A., & Taubenböck, H. (2019). Understanding an urbanizing planet: Strategic directions for remote sensing. *Remote Sensing of Environment*, 228, 164–182. 10.1016/j.rse.2019.04.020